

Geochemistry, Geophysics, Geosystems

TECHNICAL REPORTS: METHODS

10.1029/2020GC009399

Key Points:

- Bayesian algorithm capable of optimizing existing thermodynamic models to account for new observational constraints
- Experimentally determined phase equilibria are reproduced with minor refinements to existing thermodynamic model
- Revised bounds for seismic velocity and density profiles in the Martian mantle

Supporting Information:

Supporting Information may be found in the online version of this article.

Correspondence to:



D. Khan,
dean.khan@erdw.ethz.ch

Citation:

Khan, D., Liebske, C., & Connolly, J. A. D. (2021). An algorithm for thermodynamic parameter optimization: Application to the Martian mantle. *Geochemistry, Geophysics, Geosystems*, 22, e2020GC009399. <https://doi.org/10.1029/2020GC009399>

Received 27 AUG 2020
 Accepted 8 APR 2021

An Algorithm for Thermodynamic Parameter Optimization: Application to the Martian Mantle

D. Khan¹ , C. Liebske¹, and J. A. D. Connolly¹ 

¹Institute of Geochemistry and Petrology, ETH Zürich, Zurich, Switzerland

Abstract The compilation of thermodynamic models for geophysical applications is such a tedious and complex process that it is generally impractical for researchers to refit parameters in existing models in light of new constraints. To mitigate this difficulty, we develop a Bayesian algorithm that permits the modification of a thermodynamic model to account for additional observational constraints. This algorithm can be applied to any thermodynamic dataset and can utilize a wide variety of experimental constraints. To demonstrate the applicability of the algorithm it is used to revise the Stixrude and Lithgow-Bertelloni (2011, <https://doi.org/10.1111/j.1365-246x.2010.04890.x>), whole-mantle terrestrial thermodynamic model, using phase equilibrium constraints provided by Bertka and Fei (1997, <https://doi.org/10.1029/96jb03270>), for the more iron-rich compositions that are thought to be relevant to the Martian mantle. The revised thermodynamic model provides a more reliable prediction of phase equilibria in the Martian mantle. Seismic properties are calculated in an internally self-consistent manner along hot and cold areotherms to constrain the upper and lower bounds of these properties for different bulk silicate Mars compositional models.

Plain Language Summary Thermodynamic models capable of predicting geophysical properties, such as seismic wave velocities and density are useful in determining the structure of planetary interiors. We have developed an algorithm capable of refining parameters in thermodynamic models in light of new experimentally determined constraints. This algorithm is applied to the widely used Stixrude and Lithgow-Bertelloni (2011, <https://doi.org/10.1111/j.1365-246x.2010.04890.x>), thermodynamic model with data for a Mars-like composition and pressure-temperature conditions. Our results show that small changes to the thermodynamic dataset can result in a marked improvement in the agreement between the predicted and experimental results, providing estimates for geophysical properties that are consistent with experimental data. This will enable us to more reliably constrain the composition of the Martian mantle from the seismic data provided by NASA's InSight mission.

1. Introduction

Thermodynamic models for geologically relevant chemical compositions are a valuable resource in predicting the physical and thermochemical properties of planetary interiors. These models typically focus on either phase equilibria (Holland & Powell, 1998; Holland et al., 2013; Wood & Holloway, 1984) or physical properties (Angel et al., 2017; Duffy & Anderson, 1989; Weidner, 1985) with some hybrid models considering both sets of properties (Cammarano et al., 2003; Hacker et al., 2003; Ita & Stixrude, 1992; Stixrude & Lithgow-Bertelloni, 2011). The latter set of models is frequently used in conjunction with geophysical observations to infer thermochemical structures. Geophysical data provide constraints on the physical properties of phases at depth, and if compared with calculated properties of stable mineral assemblages for given pressure, temperature, and composition (P-T-X) conditions determined by Gibbs energy minimization (Bina, 1998; Connolly, 2017; de Capitani & Brown, 1987; Saxena & Eriksson, 1983; Stixrude & Lithgow-Bertelloni, 2011; Wood & Holloway, 1984), additional information of the state of planetary interiors can be obtained (Bagheri et al., 2019; Khan et al., 2018).

Phase equilibrium computations require comprehensive thermodynamic data. Sources of such data include heat measurements by calorimetry (Akaogi et al., 2002; Dachs & Geiger, 2019; Robie & Hemingway, 1995; Yusa et al., 1993), volume determinations at high pressures and temperatures of single phases to constrain equation of state (EoS) parameters (Kurnosov et al., 2017; Mao et al., 2015; Murakami et al., 2009), and equilibrium experiments of multi-phase assemblages (Frost et al., 2001; Hidayat et al., 2017).

Experimentally determined phase equilibria provide information on the relative thermodynamic properties of the phases involved, and this information is key to the refinement of thermodynamic data. Methods for such refinements, which include regression (REG), linear programming (LP), and mathematical programming (MAPS), assume that the stable assemblage has the lowest possible free energy, with experiments bracketing the P-T conditions for stable mineral assemblages. REG utilizes a system of linear equations to determine endmember contributions to system properties (Holland, 1989). The weighted mid-points of brackets are used to minimize the effect endmembers with large variances on the final result. LP calculates properties through a system of linear inequalities which provide bounds on the acceptable values of parameters, while MAPS allows for non-linear constraints (Berman et al., 1986; Gordon, 1973).

Inconsistencies among thermodynamic models can be attributed to the different data sources used to calculate parameters. Even with consistent data sources, differences in global fitting algorithms may result in different locally predicted stable assemblages required to minimize the global fitting criteria. Predicted stable assemblages can deviate considerably from experimental data and are of particular concern for compositions beyond the range considered during the calibration of the thermodynamic database, as parameters were not directly optimized for these compositions.

Local inconsistencies pose a serious problem for the drawing of inferences from geophysical data. For example, reliably reproducing the olivine-wadsleyite and ringwoodite-perovskite + ferropericlase transitions are particularly important as these represent major seismic discontinuities in the Earth and likely in other planets (Kennett & Jackson, 2009). Therefore, it is important to refine thermodynamic parameters as new experimental data becomes available to ensure an improved local consistency. Existing methods of refining thermodynamic models such as Bayesian, iterative optimization and split combination approaches can be successful in improving thermodynamic model fit to new experimental data (Chatterjee et al., 1998; Duesterhoeft & Lanari, 2020; Li et al., 2020). However, these methods are limited in the number of parameters they can successfully refine concurrently and usually focus only on experimental uncertainty to constrain parameter values, rather than exploring model parameter uncertainty more directly.

We develop an algorithm capable of revising thermodynamic data within the error established in the original assessment to improve local fitting while maintaining global consistency. To demonstrate its applicability, we use this algorithm to optimize the thermodynamic model of Stixrude and Lithgow-Bertelloni (2005, 2011) using constraints provided by the experimental data from Bertka and Fei (1997) for a Martian mantle analogue, hereafter referred to as SLB11 and BF97, respectively.

BF97 conducted a series of sub solidus multi-anvil experiments along a mantle areotherm on a FeO rich planetary mantle composition modified after Dreibus and Wanke (1985). However, comparisons of the stable phase assemblages with the predicted results by the SLB11 thermodynamic database, while consistent below 8 GPa, show significant differences at higher pressures (Figure 1). The locations of the olivine polymorph transitions vary considerably, with BF97 and SLB11 suggesting a wadsleyite-ringwoodite transition at around 15 and 17 GPa, respectively. An olivine-ringwoodite transition is observed at 13.5 GPa by BF97 while SLB11 does not predict this transition at these P-T-X conditions. There are also differences in the relative proportions of ringwoodite and majoritic garnet and the stability of majorite with increasing pressure. By refining the thermodynamic dataset, we produce a thermodynamic model that more accurately reproduces the BF97 data, while also mitigating the impact of these refinements on broader thermodynamic predictions.

To demonstrate the extent to which these changes can have an effect on physical property estimates, the revised dataset is used to reassess seismic models for the Martian mantle. This is necessary for an accurate interpretation of the seismic information collected by the InSight Mars lander (Banerdt et al., 2020; Giardini et al., 2020; Lognonne et al., 2020).

1.1. Methodology

The algorithm, written in MATLAB version R2017b, utilizes Bayesian inference to revise thermodynamic datasets (Equation 1). It does this by using least squares minimization to obtain the maximum likelihood estimate (MLE) of the parameters and their uncertainties from the new experimental constraints (Figure 2).

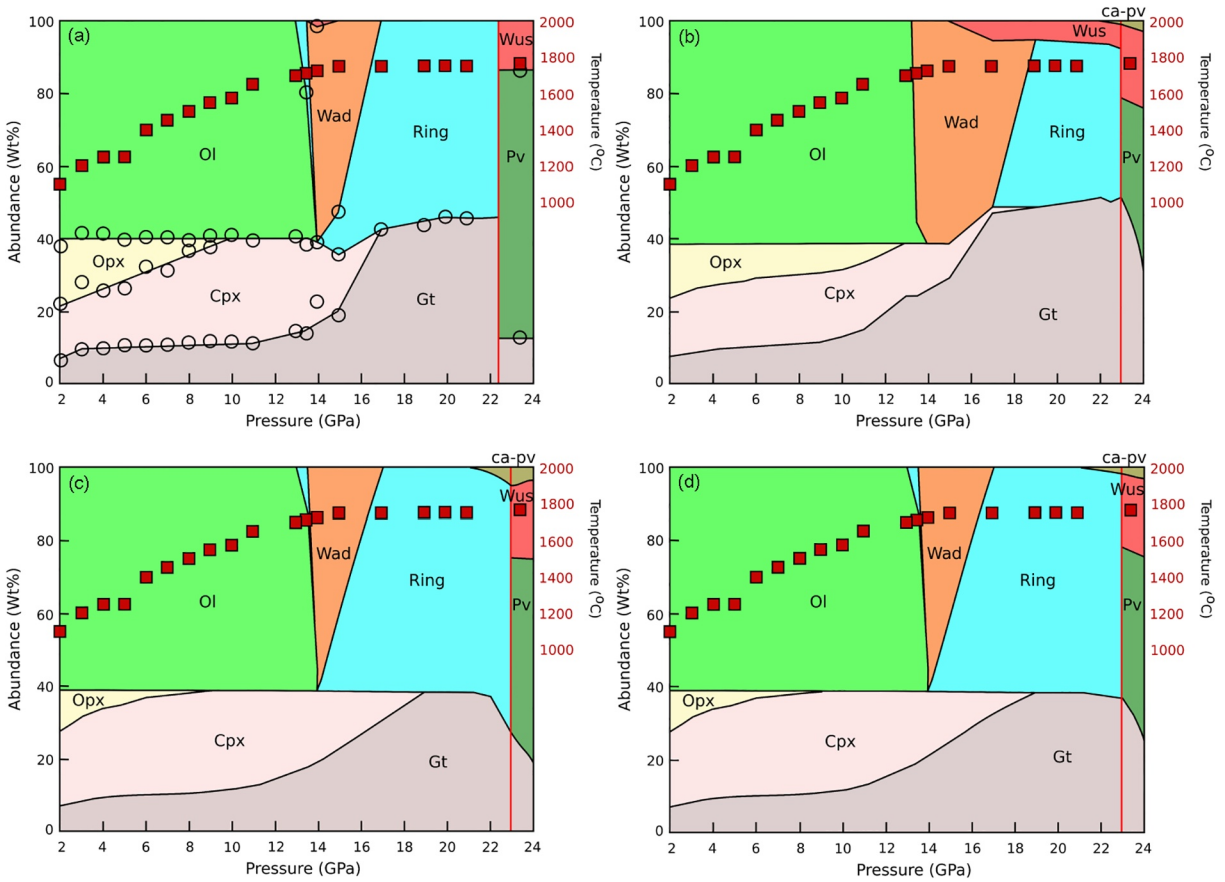


Figure 1. Pressure-abundance diagrams showing (a) averaged phase proportions calculated from Bertka and Fei (1997) data; empty circles represent the calculated phase proportions. (b) Phase equilibria predicted by SLB11, (c) MLE, and (d) the Bayesian model. Red squares show the P-T conditions of experiments. The red line marks the location of the lower mantle. (b)–(d) were calculated using *Perple_X* (Connolly, 2005). Ol, olivine; Wad, wadsleyite; Ring, ringwoodite; Opx, orthopyroxene; Cpx, clinopyroxene; Gt, garnet majorite; Pv, perovskite; ca-pv, calcium perovskite; Wus, wustite.

Bayesian inference is then applied to the MLE and a prior model (SLB11) to construct a posterior distribution, from which the Bayesian model parameters and uncertainties are determined.

$$\pi(\theta) = \frac{l(y, \theta) \cdot p(\theta)}{\int l(y, \theta) \cdot p(\theta) \cdot d\theta} \quad (1)$$

The posterior distribution $\pi(\theta)$ is the normalized product of the prior probability distribution $p(\theta)$ from SLB11 and a likelihood function $l(y, \theta)$ determined by the optimization algorithm, where y corresponds to new data not used to construct the prior. The mean and standard deviation of the posterior distribution provide the new mean and standard deviation of the parameters.

To determine $l(y, \theta)$, the user inputs the thermodynamic database to be optimized and the experimental data including errors. Gibbs energy minimization is used to calculate the equilibrium phase assemblage and its properties. A residual R_{ij} (Equation 5) is calculated for each experiment by calculating the difference between the experimentally determined results (Exp) and the predicted results (Pred) for P properties used to constrain parameters. The sum of the square of all residuals for M experiments is the objective function R_{Total} (Equation 2).

$$R_{Total} = \sum_i^M \sum_j^P (R_{ij})^2 \quad (2)$$

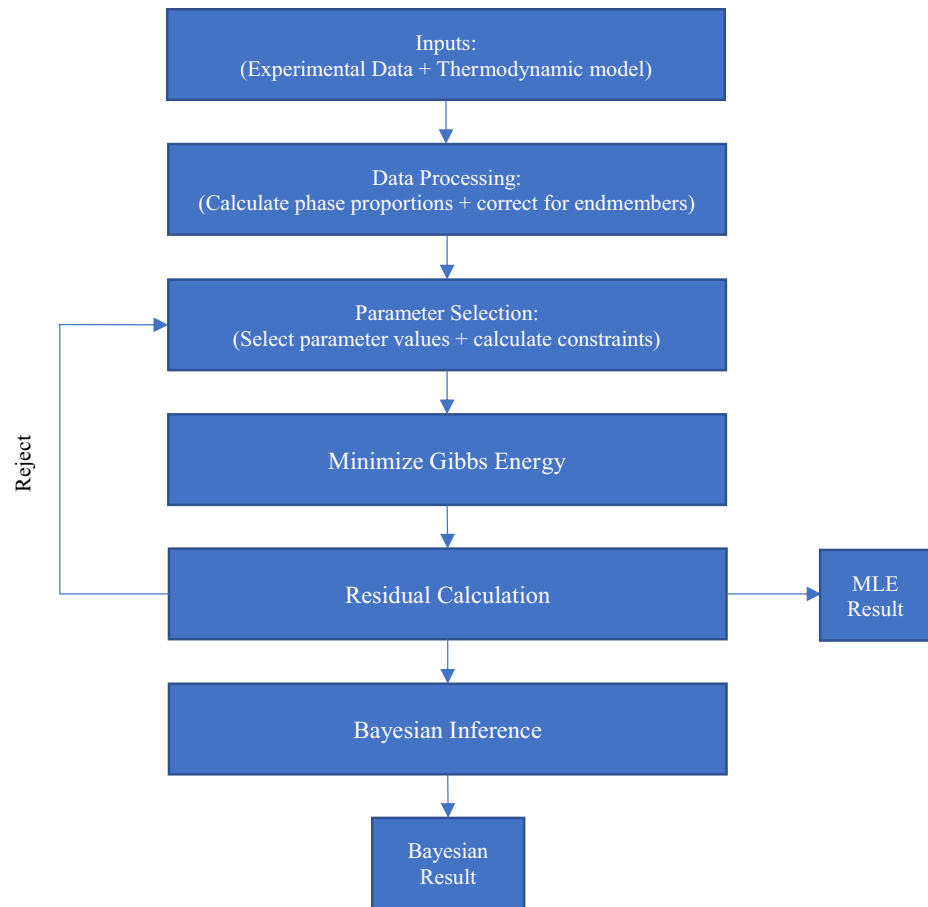


Figure 2. Flow chart showing the key steps in the optimization algorithm. Initial parameter selection is a single array containing parameter values from the prior thermodynamic model. A solution is accepted once the simplex generated by the Nelder-Mead algorithm passes the tolerance criteria. Outputs are the MLE and Bayesian result.

The optimization algorithm uses a constrained Nelder-Mead method to minimize the objective function (D’Errico, 2020; Nelder & Mead, 1965). The constrained Nelder-Mead method allows upper and lower bounds to be placed on the parameter estimates by transforming the variables into a new coordinate system between these limits, constraining the search region to within n standard deviations of the mean prior parameters. For underdetermined systems, this reduces the risk that the algorithm converges on a solution which would produce numerically unstable results outside of the P-T-X conditions of the new experimental data.

The Nelder-Mead method constructs a simplex with $n + 1$ vertices in n dimensions and successively replaces the vertex that produces the largest residual until the simplex converges on a minimum. To increase the probability that a global minimum is attained, the algorithm can be run using multiple start points over the entire parameter space. Results can also be improved by re-seeding the outputted parameter values into the optimization algorithm, until the residual can no longer be reduced. If a problem is underdetermined a unique solution is not guaranteed. The algorithm also allows the addition of new phases or phase endmembers to an existing thermodynamic model. This requires an unconstrained minimization, where no bounds are applied to the new phase parameters, to determine a set of parameter estimates consistent with the existing thermodynamic model. These values can then be used for the constrained optimization.

1.2. Application

The following methodology describes how the algorithm optimizes the SLB11 database using the BF97 experiments. Inputs from BF97 include P-T conditions of the experiments, composition of stable phases with

associated error and bulk composition as text files. The properties being minimized for are composition and volume in weight percent.

As the SLB11 database does not include all the endmembers necessary to represent the BF97 phase compositions, the BF97 compositional data is simplified. All Fe is assumed to be ferrous and minor elements from the composition of any phases for which the requisite endmembers are not in the thermodynamic model, for example, the Ca endmember for olivine, are removed and the compositions renormalized.

A mass balance relation is used to determine the phase proportions x of the stable phases for each experiment (Equation 3),

$$\mathbf{C} \cdot \mathbf{x} - \mathbf{B} = 0, \mathbf{x} \geq 0 \quad (3)$$

where \mathbf{C} is a matrix containing the compositional data of the stable phases in moles and \mathbf{B} is the bulk composition vector for the experiments. If the difference between the bulk composition estimated by mass balance and B exceeds a specified tolerance for an individual experiment, then the mass balance criterion has not been met and the compositions of the phases are adjusted by adding a weighted proportion of the missing components to all appropriate phases within compositional error until this criterion is fulfilled.

In the present optimization, seven parameters, Helmholtz free energy (F_0), Debye temperature (θ_0), Grüneisen parameter (γ_0) and its logarithmic volume derivative (q_0), bulk modulus (K_0) and its pressure derivative (K'_0) as well as chemical interaction parameters (W_{ij}), are refined as these are the most significant sources of uncertainty when determining phase equilibria (Connolly & Khan, 2016). The parameters from SLB11 are standardized to have a mean value of 0 and standard deviation of 1. The algorithm terminates when both the change in R_{Total} and the maximum change in the standardized parameters are less than 10^{-3} . The remaining EoS parameters, volume (V_0), shear strain derivative (η_{s0}), shear modulus (G_0), and its pressure derivative (G'_0), are not optimized as the Bertka and Fei (1997) experiments do not provide appropriate seismic velocity or volumetric data needed to constrain these values. Pressure (P) and temperature (T) can also be treated as variables with errors determined by the experimental run conditions. Gibbs energy minimization calculations are done using the Perple_X program “*meemum*” (Connolly, 2009) at the P-T conditions of the experiments.

A weighted residual R_w is calculated for each matching phase X and property being minimized, for example, composition, volume, seismic velocity, etc. (Equation 4).

$$R_w = \frac{\left| \left(X_j^{\text{Exp}} - X_j^{\text{Pred}} \right) \right|}{\alpha * \sigma_{\text{Exp}}} \quad (4)$$

where α is a user-defined weighting factor. If the difference between the experimental and predicted properties exceeds 1 for a given phase then $R_w = 1$. For composition, X is a vector containing the cations of each compound normalized to the ideal stoichiometry of the phase they are present in, rather than a scalar.

The total residual for each property of an experiment is then the average R_w for all matching phases plus the number of non-matching phases R_N (Equation 5).

$$R_{ij} = \frac{1}{N} \sum R_w + R_N \quad (5)$$

Once the Nelder-Mead algorithm has converged on a solution, the covariance matrix at the minimum is calculated (Equation 6).

$$\text{Cov} = \frac{y_{\text{Min}}}{D} * H^{-1} \quad (6)$$

where H^{-1} is the inverse Hessian matrix, y_{Min} is the minimum function value, and D is the difference between the number of experiments and the number of parameters being optimized. If the system is underdetermined then we assume D is 1. If the Hessian matrix is not positive definite, a pseudo-inverse is taken. If

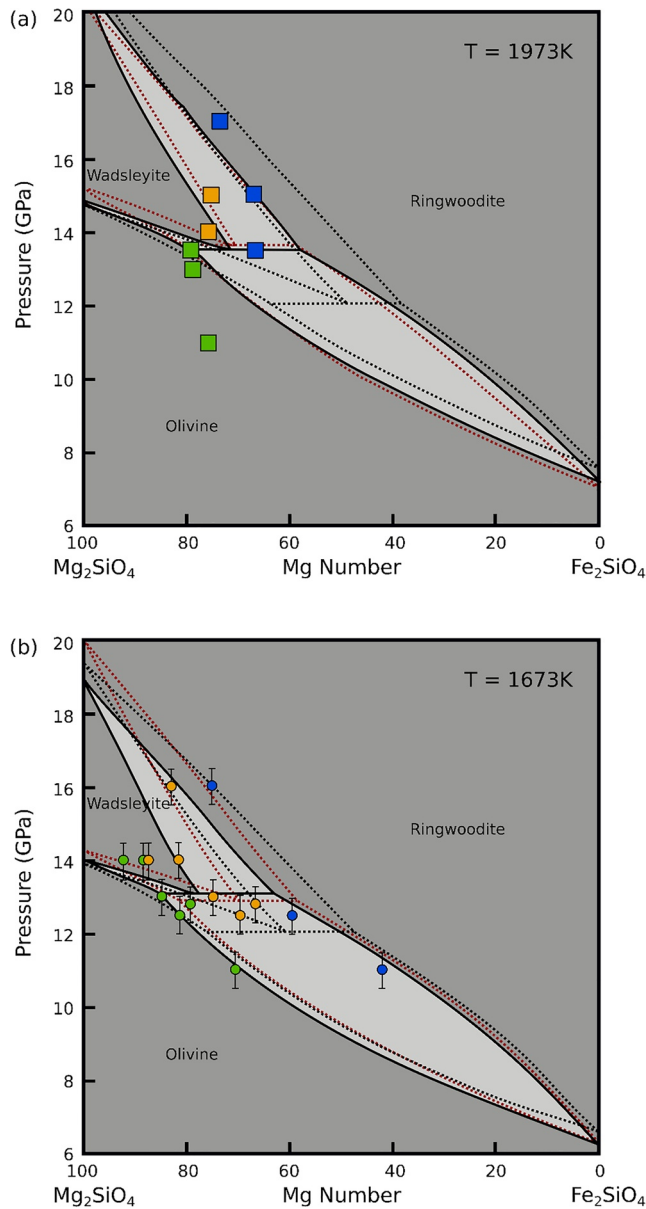


Figure 3. Comparison of the predicted phase stabilities of the olivine polymorphs from thermodynamic models (a) at 1973 K, against experimental data from Bertka and Fei (1997) and (b) at 1673 K, against experimental data of Frost (2003). Phase diagrams are calculated using *Perple_X* (Connolly, 2005). Solid black lines use the Bayesian result of this study, black dotted lines are predicted using SLB11, and red dotted lines are the phase relations shown in Bertka and Fei (1997) and Frost (2003) by fitting the experiments from those papers. Green, orange, and blue circles represent olivine, wadsleyite, and ringwoodite, respectively.

demonstrates the closeness of fit of the Bayesian result to the experimental data (Figure 3). Additionally, comparing the quality of the fit to other experiments in the same system, such as those of Frost (2003), show considerable improvements when compared with SLB11. While SLB11 is generally consistent with the thermodynamic model and experimental data of Frost and BF97, it struggles at intermediate iron concentrations to reproduce the olivine polymorph triple point at the experimentally determined pressures and

only a partial covariance matrix can be determined, the nearest semi-positive definite Hessian matrix is used instead (Higham, 1988).

Since a covariance matrix for SLB11 is not available, the covariance matrix of the MLE is assumed to also be diagonal. The probability density of the prior and likelihood are assumed to be Gaussian, thus the posterior probability distribution is also Gaussian with mean and covariance E and V (Equations 7 and 8).

$$E = V_1(V_0 + V_1)^{-1} E_0 + V_0(V_0 + V_1)^{-1} E_1 \quad (7)$$

$$V = V_1(V_0 + V_1)^{-1} V_0 \quad (8)$$

where 0 is the prior and 1 is the MLE. These values are then normalized to give the posterior probability density function.

The mean and standard deviation of the MLE and posterior distribution are the mean and standard deviation of the MLE and Bayesian result (Figure 2). The Bayesian result is used for later calculations and is available as text files formatted for use in *Perple_X*.

2. Results and Discussion

Ideally when applying this algorithm, the user will have provided a prior with a full covariance matrix and an overabundance of experimental data to sufficiently constrain parameters. This unfortunately may not always be feasible, particularly when trying to refine larger thermodynamic datasets. We demonstrate that even when applying this algorithm in a less ideal way, a Bayesian approach provides a more appropriate solution than simply fitting parameters to experiments, as by incorporating the prior it maintains a general agreement with the experimental data without entirely compromising global consistency. We compare the predicted phase equilibria for the prior, likelihood, and posterior at the bulk composition from BF97 as well as for a bulk silicate Earth composition. We also consider how predicted seismic velocities and densities differ between these models for other bulk silicate Mars compositions. The full set of Bayesian parameters can be found in the supplementary material.

2.1. Phase Equilibria

Applying our algorithm to the SLB11 database shows a marked improvement in the predicted phase assemblages when compared with those predicted using SLB11 (Figure 1). After one iteration, the simplex converges on a local minimum producing a suboptimal result which is rejected. Reseeding these parameters results in a further reduction of the objective function, improving the fit (1E, 1F). Comparing the predicted olivine polymorph stability from BF97, SLB11 and the Bayesian result further

temperatures. The location of the triple point predicted by the Bayesian result is very similar to the best fit thermodynamic models of BF97 and Frost.

However, the Bayesian result is less able to reproduce the wadsleyite phase stability field predicted by Frost (2003), due to the limited data provided by BF97. There also remains difficulties in reproducing lower mantle phase abundances and the relative stabilities of some phases for the same reasons. Inaccuracies in observed versus predicted phases related to lower mantle phase stability are a result of only one experiment from BF97 being in this P-T range. Additionally, the thermodynamically modeled results produced by the SLB11 parameters and the Bayesian parameters suggest ca-pv stability in the lower mantle, while BF97 state that this should not be the case as ca-pv should form at higher pressures in more iron-rich compositions. This could be because the SLB11 perovskite model does not contain a CaSiO_3 endmember, and therefore cannot perfectly reproduce the BF97 perovskite composition, which contains 3.59 wt% CaO. A solid solution between CaSiO_3 and $(\text{Mg, Fe})\text{SiO}_3$ at these conditions may be sufficient to suppress formation of Ca-perovskite until higher pressures are achieved.

Phase diagram sections calculated using the SLB11, MLE, and the Bayesian parameters for a bulk composition different to the one used for optimization demonstrate the extent to which stability fields can change (Figure 4). For the bulk silicate Earth composition of McDonough and Sun (1995), the majority of phase stability fields remain consistent between the prior and posterior with some small P-T offset. Most importantly those fields containing phases not observed in the experiments, such as stishovite and akimotoite, are in relatively similar positions. Differences between the Bayesian and SLB11 pseudosections are as anticipated from the observed differences between BF97 and SLB11 predictions. BF97 shows a marked decrease in Opx stability, with Opx disappearing at 10 GPa rather than 13 GPa as predicted by SLB11. This is reflected in Figure 4 by the increase in the size of the O + Cpx + Gt field at the expense of the O + Opx + Cpx + Gt field (Fields 3 and 4, respectively). Fields containing ringwoodite are more stable at lower pressures and higher temperatures in the Bayesian model, with the size of fields containing both wadsleyite and ringwoodite increasing at the expense of the wadsleyite stability field.

The differences between the posterior and the prior (Figure 4), particularly at low pressures and temperatures show some of the limitations of this approach when faced with an underdetermined problem. Attempts to destabilize Opx with a lack of information constraining its parameters at lower P-T conditions, result in a less appropriate MLE, which affects the Bayesian result. The quality of the Bayesian result is only as good as the quality of the information used to calculate it and these issues are more apparent the further away you go from the experimental P-T-X conditions used. However, since the Bayesian result also includes information from the prior, it still provides a more generally applicable thermodynamic model than the MLE results. When dealing with underdetermined problems these limitations can be overcome by increasing the number of experimental constraints, reducing the size of the optimization bounds, or by increasing the estimated covariance from the MLE results of poorly constrained parameters to reflect the lack of information.

2.2. Seismic Properties

The differences in predicted olivine polymorph phase stability at these pressure-temperature-composition (P-T-X) conditions have implications for the seismic velocity and density profiles of the Martian mantle, which is assumed to have a bulk Mg# of between 0.72 and 0.79 (Yoshizaki & McDonough, 2020). The upper and lower bounds for seismic velocity and density for nine bulk silicate Mars compositions were determined using the Bayesian result (Figure 5). Velocities were calculated along hot and cold areotherms following Verhoeven et al. (2005) using Voigt-Reuss-Hill bounds on elastic moduli.

These results suggest that the olivine-wadsleyite transition is somewhere between 12 and 14 GPa, with compositional differences having a greater effect on the depth of this transition at higher temperatures. A smaller increase in seismic velocity may be observed at lower temperatures at around 10 GPa representing the loss of Opx in the mantle. At higher temperatures, this occurs immediately before the olivine-wadsleyite transition. For simplicity, the core size was assumed to be 1389 km as this produces a mantle with a core-mantle boundary pressure of 24 GPa, covering the entire range of experimental data provided in BF97. Since all models were run along areotherms up to 24 GPa, a lower mantle is present in every model. The

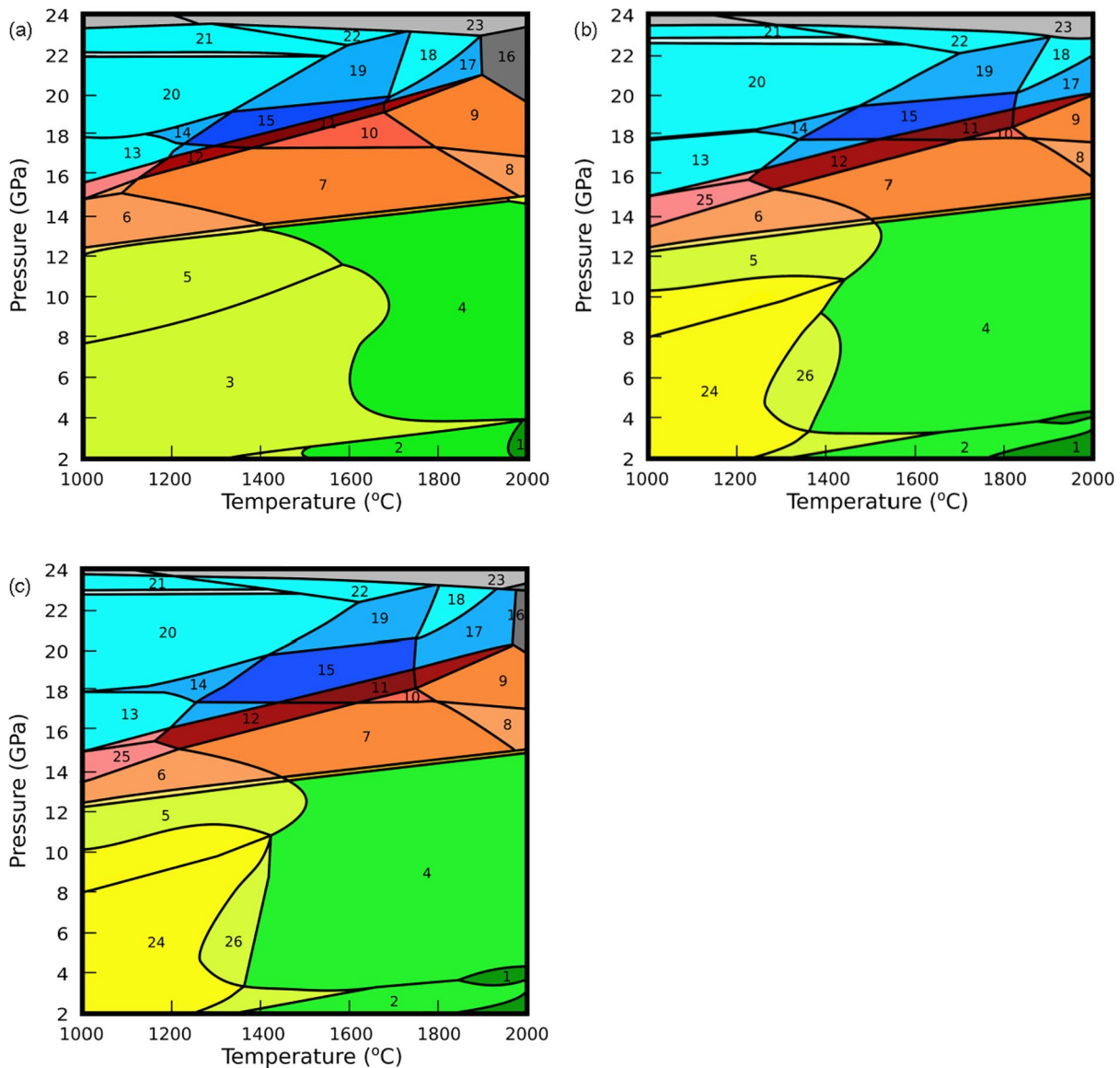


Figure 4. Phase diagrams showing differences in predicted stable assemblages by SLB11 parameters (a) and the results from this study for a simplified bulk silicate Earth (McDonough & Sun, 1995) as implemented in *Perple_X* (Connolly, 2005). (b) The pseudosection generated using the MLE and (c) the pseudosection generated using the Bayesian result. Most deviations between the prior and posterior models are as expected based on the experimental data used for the optimization, with some caveats. The large fields where Cpx + Cpx are stable in (b) demonstrates how overfitting parameters in a narrow P-T-X range, without sufficient constraints, can affect the quality of the Bayesian result globally. **1.** O + Cpx; **2.** O + Opx + Cpx; **3.** O + Opx + Cpx + Gt; **4.** O + Cpx + Gt; **5.** O + Cpx + Gt + C2/c; **6.** Wad + Cpx + Gt + C2/c; **7.** Wad + Cpx + Gt; **8.** Wad + Cpx + Gt + Wus; **9.** Wad + Gt + Wus; **10.** Wad + Gt; **11.** Wad + Ring + Gt; **12.** Wad + Ring + Cpx + Gt; **13.** Ring + Cpx + Gt + St; **14.** Ring + Gt + St; **15.** Ring + Gt; **16.** Gt + Wus; **17.** Ring + Gt + Wus; **18.** Ring + Gt + Wus + ca-pv; **19.** Ring + Gt + ca-pv; **20.** Ring + Gt + ca-pv + St; **21.** Ring + Gt + ca-pv + Aki; **22.** Ring + Gt + Pv + ca-pv; **23.** Gt + Pv + Wus + ca-pv; **24.** O + Opx + Cpx + Cpx + Gt; **25.** Wad + Ring + Cpx + Gt + C2/c; **26.** O + Cpx + Cpx + Gt.

transition from upper to lower mantle occurs at pressures greater than 23 GPa regardless of model used or P-T-X conditions. The start of the lower mantle is determined almost exclusively by pressure, rather than composition or temperature and occurs around 23.5 ± 0.3 GPa. Significant jumps in density correlate with phase transitions, but beyond that are relatively well constrained regardless of temperature.

For a fixed composition, estimated seismic velocity profiles show small differences in V_p and V_s wave speeds below 13 GPa, between the Bayesian result and SLB11 (Figure 6). Noticeable deviations in velocities occur between 13 and 17 GPa in the mantle transition zone. At the olivine-wadsleyite/ringwoodite and wadsleyite-ringwoodite phase transitions, V_p and V_s wave speeds can vary by as much as 0.2 km/s between models,

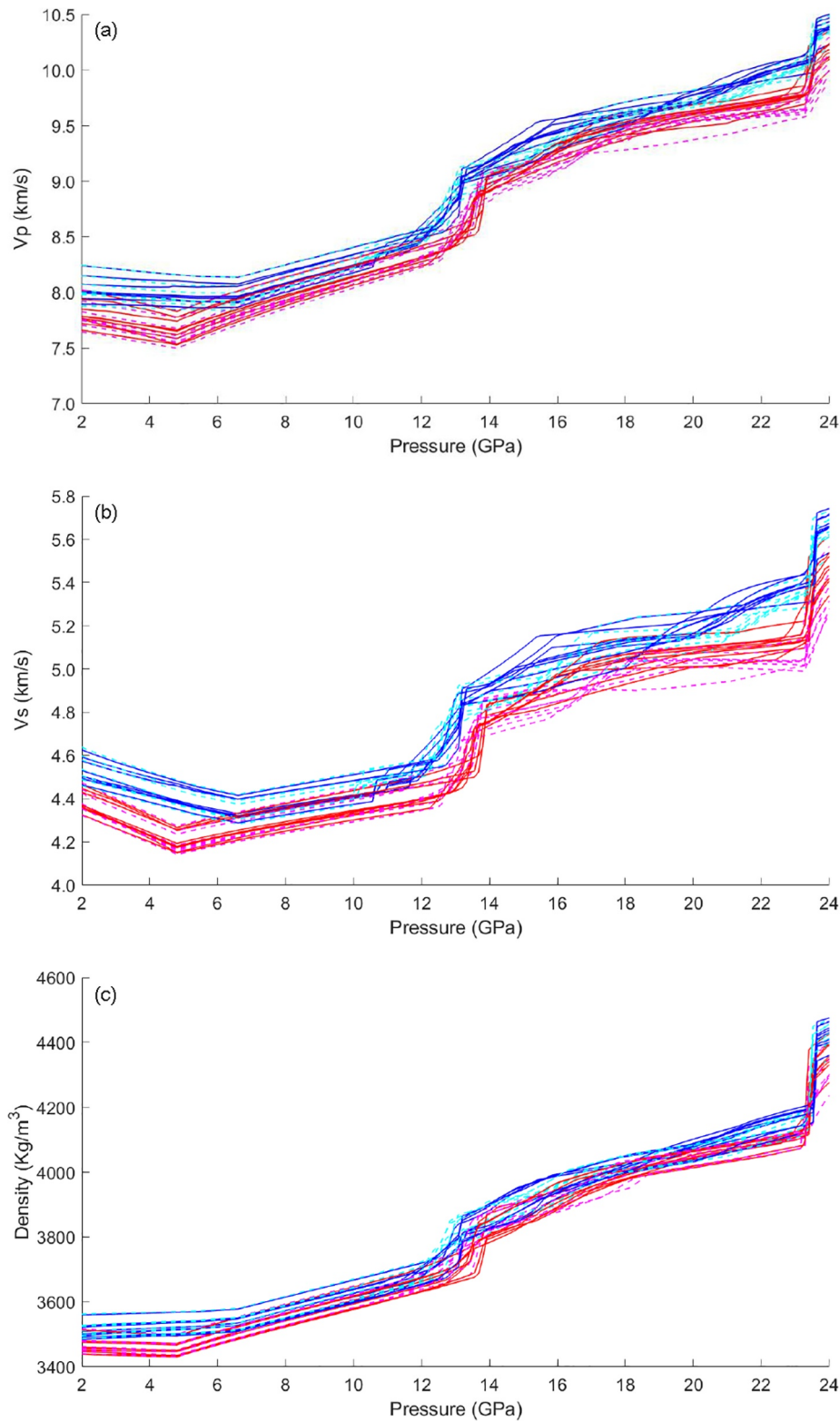


Figure 5. Plots of pressure against V_p , V_s , and density, calculated in *Perple_X* using *werami* for SLB11 (dashed) and the Bayesian result (solid) (Connolly, 2005). Nine bulk silicate Mars analogs: Morgan and Anders (1979); Ohtani and Kamaya (1992); Wanke and Dreibus (1994); Lodders and Fegley (1997); Sanloup et al. (1999); Mohapatra and Murty (2003); Khan and Connolly (2008); Taylor (2013); Yoshizaki and McDonough (2020) are tested along a hot and cold areotherm (Verhoeven et al., 2005) to determine the upper and lower bounds for these properties. Red lines are along a hot areotherm and blue lines are along a cold areotherm.

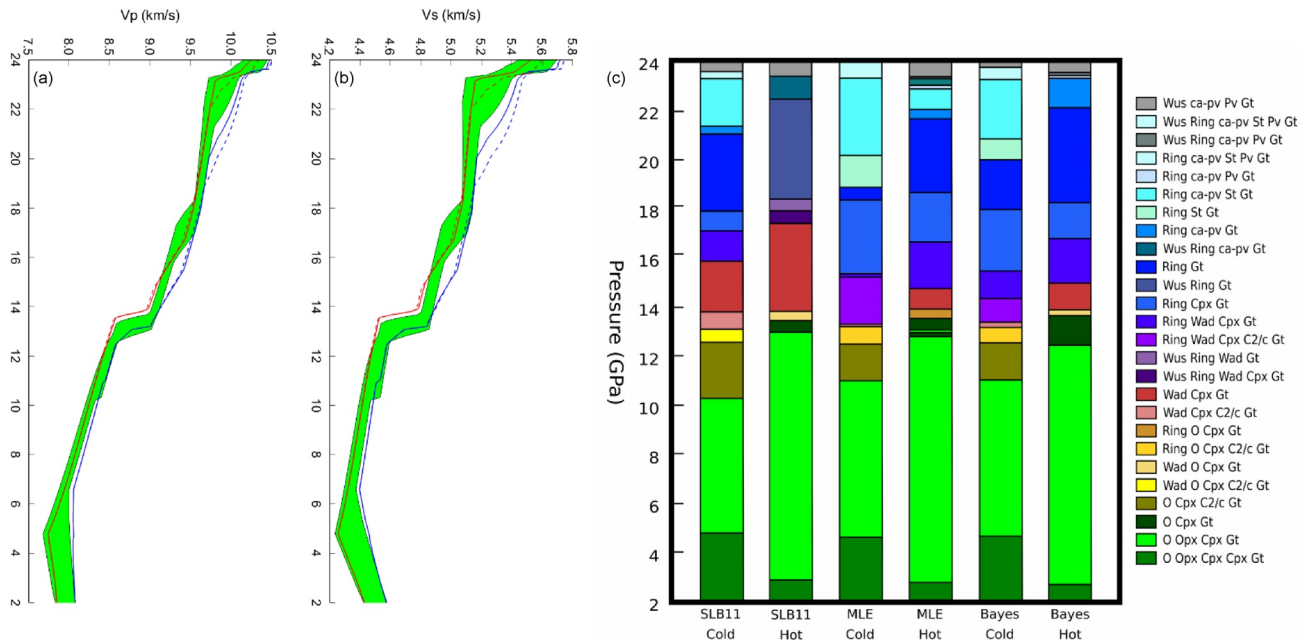


Figure 6. Vp (a) and Vs (b) wave velocity profiles with associated 1-d compositional diagrams (c) for the Yoshizaki and McDonough (2020) bulk silicate Mars analogue along the hot and cold areotherms of Verhoeven et al. (2005). In the velocity profiles, green represents the range of wave speeds predicted by SLB11, solid lines are calculated using the Bayesian result, and dashed lines using the maximum likelihood estimate. (c) All stable phases predicted along the various areotherms for the prior, likelihood, and posterior thermodynamic models.

as the depth at which these transitions occur is typically shallower for the Bayesian models. Calculated wave speeds begin to converge again toward the lower mantle.

Estimates for bulk rock density also remain consistent between models outside of the mantle transition zone. This suggests that the changes made to parameters have not resulted in notable changes in the predicted seismic properties of individual phases, but have instead changed the relative stability of phases in critical regions of the Martian mantle. This application demonstrates that the reliable reproduction of experimentally determined phase equilibria, through fine tuning of thermodynamic datasets, can noticeably affect our predictions of seismic properties. This has significant implications for the interpretation of seismic velocity profiles used for geophysical inversions of planetary interiors.

3. Conclusions

We have developed a method which allows a flexible approach to the optimization of thermodynamic models in light of new constraints, such as new additional sets of experimental data as shown in the example application above. The algorithm employs Bayesian inference which is a valuable tool for refining thermodynamic parameters as it does not require knowledge of the data used to construct the prior. The algorithm is customizable in its use of input parameters and therefore allows a wide range of thermodynamic parameters to be improved. These refinements allow thermodynamic models to be used more reliably without insulting the integrity of the original model.

Data Availability Statement

The optimization algorithm and accompanying data files are available here: <https://doi.org/10.5281/zenodo.4572300>

Acknowledgments

The research was supported by the ETH-1017-1 grant. Parameter values used to construct figures are available in the supplementary material. Constructive comments by Bob Myhill helped to improve the manuscript.

References

Akaogi, M., Tanaka, A., & Ito, E. (2002). Garnet-ilmenite-perovskite transitions in the system $Mg_3Si_4O_{12}$ - $Mg_3Al_2Si_3O_{12}$ at high pressures and high temperatures: Phase equilibria, calorimetry and implications for mantle structure. *Physics of the Earth and Planetary Interiors*, 132(4), 303–324. [https://doi.org/10.1016/S0031-9201\(02\)00075-4](https://doi.org/10.1016/S0031-9201(02)00075-4)

Angel, R. J., Alvaro, M., Miletich, R., & Nestola, F. (2017). A simple and generalised P–T–V EoS for continuous phase transitions, implemented in EosFit and applied to quartz. *Contributions to Mineralogy and Petrology*, 172(5), 29. <https://doi.org/10.1007/s00410-017-1349-x>

Bagheri, A., Khan, A., Al-Attar, D., Crawford, O., & Giardini, D. (2019). Tidal response of Mars constrained from laboratory-based viscoelastic dissipation models and geophysical data. *Journal of Geophysical Research Planets*, 124, 2703–2727. <https://doi.org/10.1029/2019JE006015>

Banerdt, W. B., Smrekar, S. E., Banfield, D., Giardini, D., Golombek, M., Johnson, C. L., et al. (2020). Initial results from the InSight mission on Mars. *Nature Geoscience*, 13, 183–189. <https://doi.org/10.1038/s41561-020-0544-y>

Berman, R. G., Engi, M., Greenwood, H. J., & Brown, T. H. (1986). Derivation of internally-consistent thermodynamic data by the technique of mathematical programming: A review with application the system MgO - SiO_2 - H_2O . *Journal of Petrology*, 27(6), 1331–1364. <https://doi.org/10.1093/petrology/27.6.1331>

Bertka, C. M., & Fei, Y. (1997). Mineralogy of the Martian interior up to core-mantle boundary pressures. *Journal of Geophysical Research*, 102(B3), 5251–5264. <https://doi.org/10.1029/96JB03270>

Bina, C. R. (1998). Free energy minimization by simulated annealing with applications to lithospheric slabs and mantle plumes. *Pure and Applied Geophysics*, 151(2), 605–618. <https://doi.org/10.1007/s000240050132>

Cammarano, F., Goes, S., Pierre, V., & Giardini, D. (2003). Inferring upper mantle temperatures from seismic velocities. *Physics of the Earth and Planetary Interiors*, 138. [https://doi.org/10.1016/S0031-9201\(03\)00156-0](https://doi.org/10.1016/S0031-9201(03)00156-0)

Chatterjee, N. D., Krüger, R., Haller, G., & Olbricht, W. (1998). The Bayesian approach to an internally consistent thermodynamic database: Theory, database, and generation of phase diagrams. *Contributions to Mineralogy and Petrology*, 133(1–2), 149–168. <https://doi.org/10.1007/s004100050444>

Connolly, J. A. D. (2005). Computation of phase equilibria by linear programming: A tool for geodynamic modeling and its application to subduction zone decarbonation. *Earth and Planetary Science Letters*, 236(1–2), 524–541. <https://doi.org/10.1016/j.epsl.2005.04.033>

Connolly, J. A. D. (2009). The geodynamic equation of state: What and how. *Geochemistry, Geophysics, Geosystems*, 10(10). <https://doi.org/10.1029/2009GC002540>

Connolly, J. A. D. (2017). A primer in Gibbs energy minimization for geophysicists. *Petrology*, 25(5), 526–534. <https://doi.org/10.1134/S0869591117050034>

Connolly, J. A. D., & Khan, A. (2016). Uncertainty of mantle geophysical properties computed from phase equilibrium models. *Geophysical Research Letters*, 43, 5026–5034. <https://doi.org/10.1002/2016GL068239>

Dachs, E., & Geiger, C. A. (2019). Thermodynamic behavior of grossular-andradite, $Ca_3(Al_xFe^{3+}_{1-x})_2Si_3O_{12}$, garnets: a calorimetric study. *European Journal of Mineralogy*, 31(3), 443–451. <https://doi.org/10.1127/ejm/2019/0031-2827>

de Capitani, C., & Brown, T. H. (1987). The computation of chemical equilibrium in complex systems containing non-ideal solutions. *Geochimica et Cosmochimica Acta*, 51(10), 2639–2652. [https://doi.org/10.1016/0016-7037\(87\)90145-1](https://doi.org/10.1016/0016-7037(87)90145-1)

D’Errico, J. (2020). Bound constrained optimization using fminsearch. <https://doi.org/10.4995/fortmed2020.2020.11438>. <https://www.mathworks.com/matlabcentral/fileexchange/8277-fminsearchbnd-fminsearchcom> Accessed 8 March 2020.

Dreibus, G., & Wanke, H. (1985). Mars, a volatile-rich planet. *Meteoritics*, 20, 367–381.

Duesterhoeft, E., & Lanari, P. (2020). Iterative thermodynamic modeling—Part 1: A theoretical scoring technique and a computer program (Bingo-Antidote). *Journal of Metamorphic Geology*, 38(5), 527–551. <https://doi.org/10.1111/jmg.12538>

Duffy, T. S., & Anderson, D. L. (1989). Seismic velocities in mantle minerals and the mineralogy of the upper mantle. *Journal of Geophysical Research*, 94(B2), 1895–1912. <https://doi.org/10.1029/JB094iB02p01895>

Frost, D. J. (2003). The structure and sharpness of $(Mg,Fe)_2SiO_4$ phase transformations in the transition zone. *Earth and Planetary Science Letters*, 216, 313–328. [https://doi.org/10.1016/S0012-821X\(03\)00533-8](https://doi.org/10.1016/S0012-821X(03)00533-8)

Frost, D. J., Langenhorst, F., & van Aken, P. A. (2001). Fe–Mg partitioning between ringwoodite and magnesio-wüstite and the effect of pressure, temperature and oxygen fugacity. *Physics and Chemistry of Minerals*, 28(7), 455–470. <https://doi.org/10.1007/s002690100181>

Giardini, D., Lognonné, P., Banerdt, W. B., Pike, W. T., Christensen, U., Ceylan, S., et al. (2020). The seismicity of Mars. *Nature Geoscience*, 13, 205–212. <https://doi.org/10.1038/s41561-020-0539-8>

Gordon, T. M. (1973). Determination of internally consistent thermodynamic data from phase equilibrium experiments. *The Journal of Geology*, 81(2), 199–208. <https://doi.org/10.1086/627835>. <http://www.jstor.org/stable/30061145>

Hacker, B. R., Abers, G. A., & Peacock, S. M. (2003). Subduction factory 1. Theoretical mineralogy, densities, seismic wave speeds, and H_2O contents. *Journal of Geophysical Research: Solid Earth*, 108(B1), 1–26. <https://doi.org/10.1029/2001jb001127>

Hidayat, T., Shishin, D., Decterov, S. A., & Jak, E. (2017). Experimental study and thermodynamic re-optimization of the FeO - Fe_2O_3 - SiO_2 system. *Journal of Phase Equilibria and Diffusion*, 38(4), 477–492. <https://doi.org/10.1007/s11669-017-0535-x>

Higham, N. J. (1988). Computing a nearest symmetric positive semidefinite matrix. *Linear Algebra and its Applications*, 103(C), 103–118. [https://doi.org/10.1016/0024-3795\(88\)90223-6](https://doi.org/10.1016/0024-3795(88)90223-6)

Holland, T. J. B. (1989). Dependence of entropy on volume for silicate and oxide minerals: A review and a predictive model. *American Mineralogist*, 74, 5–13 1980.

Holland, T. J. B., Hudson, N. F. C., Powell, R., & Harte, B. (2013). New thermodynamic models and calculated phase equilibria in NCF-MAS for basic and ultrabasic compositions through the transition zone into the uppermost lower mantle. *Journal of Petrology*, 54(9), 1901–1920. <https://doi.org/10.1093/petrology/egt035>

Holland, T. J. B., & Powell, R. (1998). An internally consistent thermodynamic data set for phases of petrological interest. *Journal of Metamorphic Geology*, 16(3), 309–343. <https://doi.org/10.1111/j.1525-1314.1998.00140.x>

Ita, J., & Stixrude, L. (1992). Petrology, elasticity, and composition of the mantle transition zone. *Journal of Geophysical Research*, 97(B5), 6849–6866. <https://doi.org/10.1029/92JB00068>

Kennett, B. L. N., & Jackson, I. (2009). Optimal equations of state for mantle minerals from simultaneous non-linear inversion of multiple datasets. *Physics of the Earth and Planetary Interiors*, 176(1), 98–108. <https://doi.org/10.1016/j.pepi.2009.04.005>

Khan, A., & Connolly, J. A. D. (2008). Constraining the composition and thermal state of Mars from inversion of geophysical data. *Journal of Geophysical Research: Planets*, 113(E7). <https://doi.org/10.1029/2007JE002996>

Khan, A., Liebske, C., Rozel, A., Rivoldini, A., Nimmo, F., Connolly, J. A. D., et al. (2018). A geophysical perspective on the bulk composition of Mars. *Journal of Geophysical Research Planets*, 123(2), 575–611. <https://doi.org/10.1002/2017JE005371>

- Kurnosov, A., Marquardt, H., Frost, D. J., Ballaran, T. B., & Ziberna, L. (2017). Evidence for a Fe³⁺-rich pyrolytic lower mantle from (Al,Fe)-bearing bridgmanite elasticity data. *Nature*, 543(7646), 543–546. <https://doi.org/10.1038/nature21390>
- Li, X., Yang, L., Zhou, Q., Qi, T., Liu, G., & Peng, Z. (2020). A split-combination method for estimating the thermodynamic properties (Gfo and Hfo) of multicomponent minerals. *Applied Clay Science*, 185, 105406. <https://doi.org/10.1016/j.clay.2019.105406>
- Lodders, K., & Fegley, B., Jr (1997). An oxygen isotope model for the composition of Mars. *Icarus*, 126, 373–394. <https://doi.org/10.1006/icar.1996.5653>
- Lognonné, P., Banerdt, W. B., Pike, W. T., Giardini, D., Christensen, U., Garcia, R. F., et al. (2020). Constraints on the shallow elastic and anelastic structure of Mars from InSight seismic data. *Nature Geoscience*, 13, 213–220. <https://doi.org/10.1038/s41561-020-0536-y>
- Mao, Z., Fan, D., Lin, J.-F., Yang, J., Tkachev, S. N., Zhuravlev, K., & Prakapenka, V. B. (2015). Elasticity of single-crystal olivine at high pressures and temperatures. *Earth and Planetary Science Letters*, 426, 204–215. <https://doi.org/10.1016/j.epsl.2015.06.045>
- McDonough, W., & Sun, S. S. (1995). The composition of the Earth. *Chemical Geology*, 67, 1050–1056.
- Mohapatra, R. K., Murty, S. V. S., & Feb (2003). Precursors of Mars: Constraints from nitrogen and oxygen isotopic compositions of martian meteorites. *Meteoritics and Planetary Science*, 38, 225–241. <https://doi.org/10.1111/j.1945-5100.2003.tb00261.x>
- Morgan, J. W., & Anders, E. (1979). Chemical composition of Mars. *Geochimica et Cosmochimica Acta*, 43, 1601–1610. [https://doi.org/10.1016/0016-7037\(79\)90180-7](https://doi.org/10.1016/0016-7037(79)90180-7)
- Murakami, M., Asahara, Y., Ohishi, Y., Hirao, N., & Hirose, K. (2009). Development of in situ Brillouin spectroscopy at high pressure and high temperature with synchrotron radiation and infrared laser heating system: Application to the Earth's deep interior. *Physics of the Earth and Planetary Interiors*, 174(1), 282–291. <https://doi.org/10.1016/j.pepi.2008.07.030>
- Nelder, J. A., & Mead, R. (1965). A simplex method for function minimization. *The Computer Journal*, 7(4), 308–313. <https://doi.org/10.1093/comjnl/7.4.308>
- Ohtani, E., & Kamaya, N. (1992). The geochemical model of Mars: An estimation from the high pressure experiments. *Geophysical Research Letters*, 19, 2239–2242. <https://doi.org/10.1029/92GL02369>
- Robie, R., & Hemingway, B. S. (1995). Thermodynamic properties of minerals and related substances at 298.15K and 1 bar. *US Geological Survey Bulletin*, 1–461. <https://doi.org/10.3133/b2131>
- Sanloup, C., Jambon, A., & Gillet, P. (1999). A simple chondritic model of Mars. *Physics of the Earth and Planetary Interiors*, 112(1), 43–54. [https://doi.org/10.1016/S0031-9201\(98\)00175-7](https://doi.org/10.1016/S0031-9201(98)00175-7)
- Saxena, S. K., & Eriksson, G. (1983). Theoretical computation of mineral assemblages in pyrolyte and lherzolite. *Journal of Petrology*, 24(4), 538–555. <https://doi.org/10.1093/petrology/24.4.538>
- Stixrude, L., & Lithgow-Bertelloni, C. (2005). Thermodynamics of mantle minerals - I. Physical properties. *Geophysical Journal International*, 162(2), 610–632. <https://doi.org/10.1111/j.1365-246X.2005.02642.x>
- Stixrude, L., & Lithgow-Bertelloni, C. (2011). Thermodynamics of mantle minerals - II. Phase equilibria. *Geophysical Journal International*, 184(3), 1180–1213. <https://doi.org/10.1111/j.1365-246X.2010.04890.x>
- Taylor, G. J. (2013). The bulk composition of Mars. *Geochemistry*, 73, 401–420. <https://doi.org/10.1016/j.chemer.2013.09.006>
- Verhoeven, O., Rivoldini, A., Vacher, P., Mocquet, A., Choblet, G., Menvielle, M., et al. (2005). Interior structure of terrestrial planets: Modeling Mars' mantle and its electromagnetic, geodetic, and seismic properties. *Journal of Geophysical Research*, 110, E04009. <https://doi.org/10.1029/2004JE002271>
- Wanke, H., & Dreibus, G. (1994). Chemistry and accretion history of Mars. *Philosophical Transactions of the Royal Society of London. Series A, Mathematical and Physical Sciences*, 349, 285–293. <https://doi.org/10.1098/rsta.1994.0132>
- Weidner, D. J. (1985). A mineral physics test of a pyrolyte mantle. *Geophysical Research Letters*, 12(7), 417–420. <https://doi.org/10.1029/GL012i007p00417>
- Wood, B. J., & Holloway, J. R. (1984). A thermodynamic model for subsolidus equilibria in the system CaO MgO Al₂O₃ SiO₂. *Geochimica et Cosmochimica Acta*, 48(1), 159–176. [https://doi.org/10.1016/0016-7037\(84\)90358-2](https://doi.org/10.1016/0016-7037(84)90358-2)
- Yoshizaki, T., & McDonough, W. F. (2020). The composition of Mars. *Geochimica et Cosmochimica Acta*, 273, 137–162. <https://doi.org/10.1016/j.gca.2020.01.011>
- Yusa, H., Akaogi, M., & Ito, E. (1993). Calorimetric study of MgSiO₃ garnet and pyroxene: Heat capacities, transition enthalpies, and equilibrium phase relations in MgSiO₃ at high pressures and temperatures. *Journal of Geophysical Research*, 98(B4), 6453–6460. <https://doi.org/10.1029/92JB02862>